

Probing Multiscale Dissolution Dynamics in Natural Rocks through Microfluidics and Compositional Analysis

Bowen Ling^{a,b}, Mo Sodwatana^b, Arjun Kohli^b, Cynthia M. Ross^b, Adam Jew^c, Anthony R. Kavscek^b, and Ilenia Battiato^{b,†}

^aInstitute of Mechanics, Chinese Academy of Sciences, Beijing, China; ^bEnergy Resources Engineering, Stanford University, Stanford, CA, USA; ^cSLAC National Accelerator Laboratory, Menlo Park, CA, USA

This manuscript was compiled on May 25, 2022

1 **Mineral dissolution significantly impacts many geological systems. Carbon released by diagenesis, carbon sequestration, and acid injection are**
 2 **several examples where geochemical reactions, fluid flow, and solute transport are strongly coupled. Yet, the dynamics of mineral dissolution**
 3 **and fluid-solid interaction remain poorly understood. The complexity in these systems involves interplay between various mechanisms that**
 4 **operate at time scales ranging from microseconds to years. Current experimental techniques only characterize dissolution processes using**
 5 **static images that are acquired with long measurement times and/or low spatial resolution. These limitations prevent direct observation of how**
 6 **dissolution reactions progress within an intact rock with spatially heterogeneous mineralogy and morphology. We utilize microfluidic cells**
 7 **embedded with thin rock samples to visualize dissolution with significant temporal resolution (100 ms) in a large observation window (3×3**
 8 **mm). In this study, we injected acidic fluid into eight shale reservoir rock samples ranging from 8 to 86 wt % carbonate minerals. The pre- and**
 9 **post-reaction microstructures are characterized at the scale of pores (0.1 - 1 μm) and fractures (1 - 1000 μm). We observe that non-reactive**
 10 **particle exposure, fracture morphology, and loss of rock strength are strongly dependant on both the relative volume of reactive grains and**
 11 **their distribution. Time-resolved images of the rock cell unveil the spatiotemporal dynamics of dissolution, including two-phase flow effects, in**
 12 **real-time and illustrate the changes in the fracture interface across the range of sample composition. Moreover, the dynamical data provide a**
 13 **new approach for characterizing reactivity parameters of natural heterogeneous samples, when porous media effects are not negligible. The**
 14 **newly developed platform and experimental workflow provides real-time characterization of geochemical reactions and has the potential to**
 15 **inform various subsurface engineering processes.**

Dissolution | Microfluidics | Geochemistry | Mineralogy

1 **A** number of studies indicate that both natural and anthropogenic carbonate
 2 **dissolution contributes to global carbon emissions (1, 2), cap rock destabilization**
 3 **at CO₂ sequestration sites (3), mobilization of heavy metal elements in groundwater**
 4 **(4), fracture collapse within reservoirs (5), and heavy metal bioavailability in soils**
 5 **(6). Dissolution in geologic systems is often comprised of a chain of geochemical**
 6 **reactions controlled by solid and fluid interactions, fracture and porosity evolution,**
 7 **and reactive solute transport (7). As reactions progress, the fluid chemistry is**
 8 **impacted by flow and reactive solute availability. In turn, the flow and concentration**
 9 **fields are altered as the fracture and pore geometry evolve via dissolution that is**
 10 **controlled by the mineralogy and heterogeneity of the rock (8, 9). Controlling and**
 11 **optimizing various subsurface processes (8–14) requires an experimental platform**
 12 **that captures both the real-time dynamics of dissolution and provides insight into the**
 13 **coupling and feedbacks between different physical processes. Yet, the inherent multi-**
 14 **physics nature of reactive transport in rocks is only one of the challenging aspects**
 15 **of studying such systems by direct observation. These strongly coupled and highly**
 16 **localized physical phenomena often occur on vastly different characteristic spatial**
 17 **and temporal scales. For example, the spatial scales associated with advective mass**
 18 **transport in fractures may be much larger than the characteristic scale of reactive**
 19 **mass transport at the rock surface. Such a disparity in scales requires that the**

20 experimental techniques used to probe the dynamic feedbacks of reactive transport
21 in natural samples have both high temporal- and spatial-resolution, and maintain a
22 significant field of view to capture both (i) physical-chemical processes over multiple
23 spatial and temporal scales, as well as (ii) the sample's mineralogical heterogeneity.
24 Achieving high temporal resolution and large fields of view during dissolution
25 processes, in combination with compositional information, is critical to investigate
26 a number of open scientific questions in the context of rock weathering kinetics:
27 What is the impact of spatial heterogeneity and reactive surface accessibility on
28 reaction rates and porosity-surface area correlations in real rock samples? Can these
29 effects be quantified in laboratory setups and incorporated in reactive transport
30 models? Although dynamic models for porosity and surface evolution are critical to
31 assess reactivity, they are incredibly difficult to constrain, particularly in natural
32 heterogeneous samples, where porous media effects may be major. (15–17).

33 Generally, a trade-off exists between spatial and temporal resolution in dissolution
34 experiments. Non-optical experimental techniques, e.g. X-ray microtomography
35 (μ CT) and scanning electron microscopy (SEM), provide structural and mineral
36 information at sub-micron scales (18–20); however, these methods each have draw-
37 backs with respect to characterizing dynamically in-situ dissolution, because of
38 long acquisition times for μ CT (21) and the need to keep samples under vacuum
39 conditions for SEM (22). Dissolution reactions can occur within microseconds after
40 the reactive fluid reaches soluble minerals and can continue interacting with the

Significance Statement

Dissolution reactions are ubiquitous in many geological systems. The interactions between rocks and acidic fluids are complex, dynamic, and dependent on rock properties and morphology. Physical processes with vastly different time and spatial scales may occur simultaneously, presenting challenges for current experimental techniques. Here, we propose a new platform for probing dissolution dynamics in which natural samples are embedded in microfluidic cells and are imaged combining both high-speed camera data acquisition techniques and SEM-BSE and EDS imaging to characterize dissolution processes at a very high spatial (0.1-1 μ m) and temporal (0.1s) resolution over large fields of view (mm). The newly designed platform allows for both in situ optical imaging and ex situ electron microscopy. The static and dynamic image data provide a direct mechanistic understanding of dissolution over a range of temporal and spatial scales.

Please provide details of author contributions here.

† To whom correspondence should be addressed. E-mail: ibattiat@stanford.edu

41 minerals for days. Documenting dissolution dynamics of real rocks at relevant scales
42 requires an in situ platform with large temporal resolution and significant fields of
43 view. Yet, high resolution imaging is restricted by sample size and/or the camera's
44 field of view.

45 Microfluidic devices have been rapidly evolving to meet growing experimental
46 needs and can be imaged using cameras with fast frame rates (23–26). Consequently,
47 applications of microfluidic devices provide new opportunities to study dissolution
48 reaction mechanisms and the strong influence brought by fluid flow. For example,
49 Song et al. (26) designed a calcite-functionalized microfluidic device to study multi-
50 phase reactive systems at the pore-scale. Soullaine et al. (23) engineered a calcite
51 grain bearing microfluidic cell within which the dissolution process is recorded at
52 high temporal resolution. Dynamical dissolution data show the interaction between
53 flow and reactive transport, while providing experimental benchmarks for theoretical
54 and numerical model development. Yet, geological formations exhibit significant
55 physico-chemical heterogeneity whose complexity cannot be captured by synthe-
56 sized materials (e.g. CaCO_3). Natural samples are usually highly heterogeneous
57 in composition (27–29), fracture morphology (30–32), and mineral distribution
58 (23, 33, 34). Moreover, as dissolution reactions generate additional phases in the
59 fluid (e.g., gases), the hydrodynamics of these systems depend strongly on the
60 surface properties, such as the wettability and the topology of mineral surfaces,
61 which synthetic materials do not replicate.

62 Recent studies that integrate natural samples into microfluidics have improved
63 our understanding of the fundamentals of fluid-solid interactions and reactive
64 transport in subsurface environments (35–38). Deng et al. (36) show an *in operando*
65 synchrotron system based on a micromodel coupled with real rock sample, in which
66 the reaction is recorded with spatial resolution of $1.3 \mu\text{m}$ and temporal resolution
67 15 min/frame. This study shows the significant pore space change brought by
68 dissolution reactions. However, such temporal resolution is not sufficient to study
69 the real-time interplay between dissolution reactions and morphological changes of
70 the rock associated to its mineralogical heterogeneity and fluid flow.

71 To address these limitations, we designed a sample-embedded microfluidic cell that
72 can be imaged both in situ at high temporal resolution using optical imaging and ex
73 situ at high spatial resolution using electron microscopy. The combination of such
74 techniques allows us to study multiscale multiphysics dynamic dissolution processes
75 and their interplay with flow at relevant temporal scales and large fields of view
76 (mm scale), while mapping the rock chemical heterogeneity at a much finer scale (0.1
77 μm scale). This represents the first study that incorporates correlative optical and
78 EDS imaging on the same natural sample before and after dissolution reactions. By
79 combining dynamic optical imaging and high resolution imaging and spectroscopy,

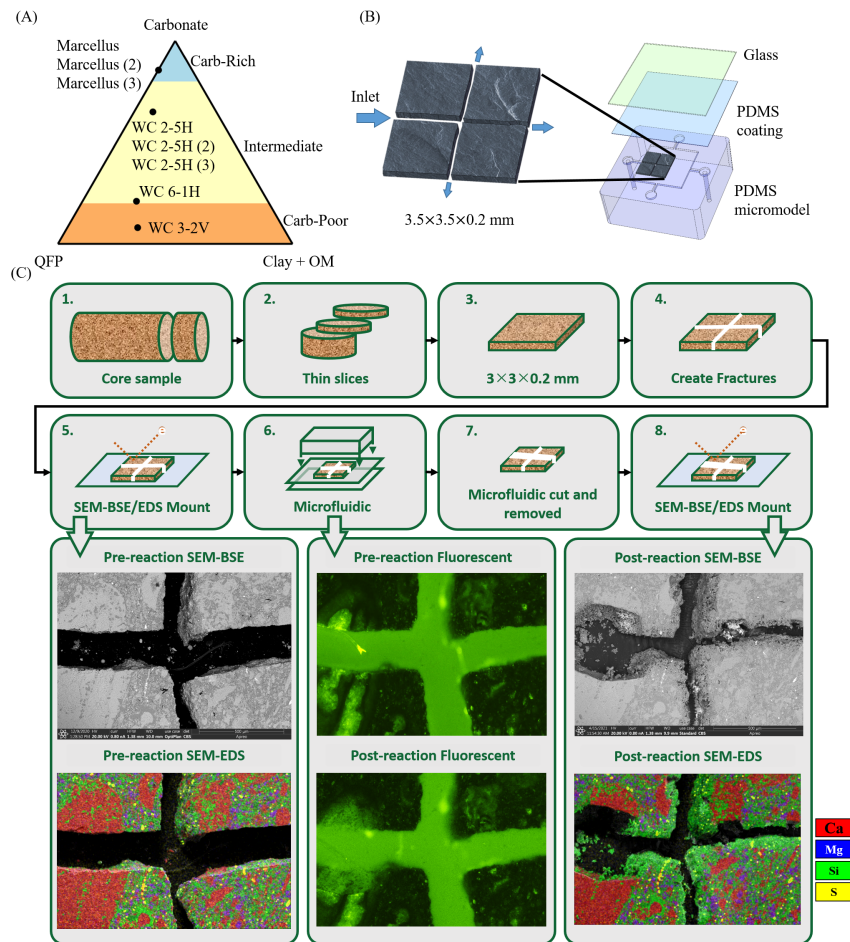


Fig. 1. (A) Compositional ternary plot of the four study samples and their replicas (Table S1. QFP - quartz, feldspar, and pyrite; OM - organic matter). The Marcellus sample is carbonate-rich. The clay-rich Wolfcamp sample, WC 3-2V, occurs at the other end of the carbonate spectrum. Two other Wolfcamp samples represent intermediate compositions. (B) Sample embedded microfluidic cell construction. Rock samples are polished into thin wafers and quartered. The pieces are placed in the flow chamber and aligned with the inlet to simulate two intersecting fractures. The glass cover used for visual access is coated with PDMS and bonded to the flow chamber. (C) Flowchart of the experimental protocol: The sample preparation starts with thin slices of core samples (1 and 2); each piece is ground and polished to a thickness of 0.2 mm (3), and then cut to 3×3 mm; We score and break the sample into four pieces (4). These four pieces are placed on a glass slide holder for pre-reaction SEM-BSE and EDS scanning (5). Afterwards, the four pieces are placed on a polydimethylsiloxane (PDMS) coated glass slide, configured to form intersecting fractures, aligned with the inlet to create a 0.2 mm fracture, and sealed in the microfluidic chip (6). The fluorescent microscopy and dynamic dissolution measurements are conducted. After the dissolution experiment, the microfluidic cell is cut open (7) and the post-reaction sample (four pieces) is moved to the SEM mount for the post-reaction SEM-based characterization (8).

80 we show that dissolution results from a tight coupling between fracture topology
 81 evolution, reaction rate heterogeneity induced by local chemical composition and
 82 mediated by fracture-scale flow, and non-reactive particle exposure. Specifically,
 83 direct SEM-BSE post-mortem visualizations of the reacted interface across shale reservoir rock samples with
 84 carbonate content ranging between 8 and 86 wt %. Our study demonstrates how the
 85 **coupling** between flow and reactive transport during acidification of shale samples
 86 with different carbonate contents is strongly controlled by the sample chemical
 87 composition and the characteristic length scale of the physico-chemical heterogeneity
 88 (i.e. carbonate grain size) **at the flow rate investigated**. Concurrent analysis of high
 89 temporal resolution images and chemical composition allows one track locally the
 90

91 impact of reactive transport and dissolution across multiple scales and visualize its
92 effects on the topological features of the altered layer. Finally, via the high temporal
93 resolution results, dynamical relationships between pore volume and mineral surface
94 area can be determined as a function of carbonate content and distribution: such
95 correlations are critical to assess reactivity in reactive transport models.

96 **Materials and Methods**

97 **Shale Samples Description and Preparation.** In this study, we employ eight shale
98 samples with carbonate content ranging from 8 to 86 wt%: three samples from the
99 Marcellus carbonate-rich shale (denoted as Marcellus, Marcellus (2) and Marcellus
100 (3)), and five samples from the Wolfcamp shale (WC 2-5H, WC 2-5H (2), WC 2-5H
101 (3), WC 6-1H, and WC 3-2V). The composition of each sample is described in the
102 ternary diagram in Figure 1(A). The same code name indicates that the samples
103 are from the same core, while the number in bracket indicates that the experiment
104 is replicated across different samples (replicas) with the same composition. The
105 shale samples contain reactive carbonate minerals such as calcite (CaCO_3) and
106 dolomite ($\text{CaMg}(\text{CO}_3)_2$), that occur as fossils, individual crystals, discrete grains,
107 and interlocking crystalline networks. In carbonate-rich samples, silicates (SiO_4 -
108 bearing minerals such as quartz) as well as other minerals are distributed in a
109 carbonate matrix. These non-carbonate minerals may be concentrated in horizontal
110 laminations or other structures. In carbonate-poor samples, carbonate minerals
111 occur as small particles that are spread sporadically throughout the matrix and,
112 in some cases, are isolated to particular structures such as horizontal laminations.
113 Although we focus on shale reservoir rocks with variable composition, small initial
114 porosity, and fine mineral grain size, the approach is directly applicable to other
115 rock types. Once collected, rock samples are first polished to the desired thickness
116 ($\sim 200 \mu\text{m}$) and cut to size $3 \times 3 \text{ mm}$; then, two fractures are scored on the sample,
117 and finally the entire piece is quartered in four pieces of approximate size $L \sim 0.75$
118 mm: L is large enough to capture the sample chemical and physical heterogeneity,
119 whose characteristic length scale is ℓ . For the carbonate-rich sample (Marcellus)
120 $\ell \gg L$ (with ℓ the size of carbonate grains); $\ell \approx L$ for the sample with intermediate
121 carbonate content (WC 2-5H); and $\ell \ll L$ for the carbonate-poor samples (WC
122 6-1H and WC 3-2V).

123 **Pre- and Post-reaction Characterization, and Sample-Embedded Microfluidic**
124 **Cell Fabrication.** Once the sample preparation is completed, each sample is charac-
125 terized pre-reaction using backscattered electron imaging (SEM-BSE) and energy
126 dispersive spectroscopy (EDS) for elemental distribution and mineral identification
127 (TFS Apreo S LoVac with Bruker Quantax 6|60 EDS detector and Esprit 2.2 soft-

ware). Once prereaction characterization is completed, the left side of the sample is inserted in the flow cell, molded from polydimethylsiloxane (PDMS) using a silicon wafer mold, and aligned with the flow chamber wall such that the sample pieces create two intersecting fractures, the fracture entrance is aligned with the microfluidic inlet, and the width of the inlet is 200 μm . To close and seal the chamber, we spin coat a glass slide with PDMS and bond it to the flow cell. With the top and bottom surfaces of the sample sealed by PDMS, the fluid can only travel through the fractures. The microfluidic device is a quasi 2-D chip with a $\sim 200 \mu\text{m}$ rock sample embedded inside a central flow chamber (Figure 1(B)). This microfluidic device allows visualization through the glass slide and captures the quasi-2D surface variation of the fractures during the dissolution experiments as detailed in the following section. After the dissolution experiment, the microfluidic chip is cut open, and the sample is moved to the glass slide for post-reaction SEM-BSE and EDS characterization. A flowchart of the experimental protocol is provided in Figure 1(C).

Microfluidic Dissolution Experiments. Dynamic flow and reactive transport experiments are performed by adopting the fluorescent microscopy visualization technique from previous studies (39–41), and following the same experimental protocol for all the samples. We first saturate the fractured samples and sample cell with de-ionized (DI) water. The saturated chip is then placed on a motorized stage and viewed using an inverted microscope (Ti-E, Nikon Instruments Inc., Melville, NY, USA). Fluorescent dye ALEXA-488 (ThermoFisher Scientific, Inc., San Diego, CA, USA) is injected before and after dissolution to enhance the boundary contrast between the pore space and the solid matrix. A compatible filter cube (C-FL GFP, Nikon Instruments Inc., Melville, NY, USA) restricts the spectrum to green/blue light only. Acid solution (1% HCl) is injected at flow rate $Q = 1000 \mu\text{L/hr}$ for 3 mins, and the valves switch to DI-water injection immediately when the acid injection is completed. This corresponds to an average velocity $U \sim 6.94 \times 10^{-2} \text{ m/s}$ inside the fracture (at the inlet), and a Péclet number $Pe = LU/D \sim 149.1$, where $L = 200 \mu\text{m}$ and $D = 9.31 \times 10^{-9} \text{ m}^2/\text{s}$ is the diffusion coefficient of H^+ in water. The Damköhler number is $Da = \alpha_{H^+} L^2/D = 1.91$, where $\alpha_{H^+} = 0.456 \text{ s}^{-1}$ is the reaction rate constant of H^+ (42). The entire injection process is recorded by a high speed camera (Hamamatsu Flash LT Monochrome, Hamamatsu, San Jose, CA, USA) that is connected to the inverted microscope, with the recording set to capture approximately 10 images per second (10 fps) with the field of view of size $3 \times 3 \text{ mm}$. For the samples in this study, the minerals dissolved by HCl are mostly calcite and some dolomite. CO_2 gas is released during the experiments and, in some cases, can be imaged. The reaction between carbonate minerals and HCl is



167 where the CO_2 may dissolve to form carbonic acid, H_2CO_3 , that may dissociate
168 into HCO_3^- , CO_3^{2-} , and H^+ . Of course, the amount of H_2CO_3 formed in solution
169 depends on pressure and temperature.

170 Results and Discussion

171 **Dynamic Imaging Results.** Dynamic dissolution images at 120-130s time intervals
172 for four of the eight experiments are shown in Figure 2. Figure 2 includes images
173 for samples with high (Marcellus), intermediate (WC 2-5H(2) and WC 2-5H (3))
174 and low (WC 3-2V)) carbonate content. Optical images for all other samples
175 are available in the Supplementary Information. All experiments, except for WC
176 2-5H(2), have corresponding pre- and post-reaction EDS data.

177 For the Marcellus (with $\ell \gg L$) and the WC 2-5H(2) and WC 2-5H(3) samples
178 (with $\ell \sim L$), substantial changes in the width, shape, and tortuosity of the
179 fractures are caused by dissolution and imaged in real time. However, while the
180 fractures widen uniformly and the roughness of the fracture surfaces remains similar
181 before and after dissolution in the Marcellus sample, in the WC 2-5H samples the
182 fractures widen substantially and heterogeneously corresponding to the occurrence
183 of carbonate grains, and the surface roughness abruptly changes after dissolution
184 (see Figure S4 of the SI).

185 Optical images of WC 2-5H(2) and WC 2-5H(3) samples reveal strong physical
186 heterogeneity, which will be characterized compositionally through SEM-BSE and
187 EDS static images in the following section. Dynamic imaging of all WC 2-5H
188 experiments show preferential reaction patterns in which large calcite regions are
189 selectively dissolved resulting in the generation of large bubbles in these areas. The
190 silicate-rich regions remain comparatively unaffected (see Figure 2, and S13-S15).
191 This is most apparent in the before and after fluorescent images in Figure S9 in the SI.
192 Instead, the carbonate-poor sample does not show any visual structural/topological
193 change at this scale. Note that, although dissolution of isolated dolomite within the
194 silicate regions adjacent to the fracture wall cannot be resolved at this magnification,
195 small bubbles are observed in these areas suggesting that dissolution may be
196 occurring (Figure 2). This observation is consistent with the pre-reaction and
197 post-reaction SEM-BSE images, which do show dissolution of isolated grains as
198 discussed in later sections (Figure 4). Overall, the high-speed large field of view
199 optical imaging allows us to visualize dynamically changes in the aperture and
200 macroscopic features of the fractures for samples with greater carbonate content

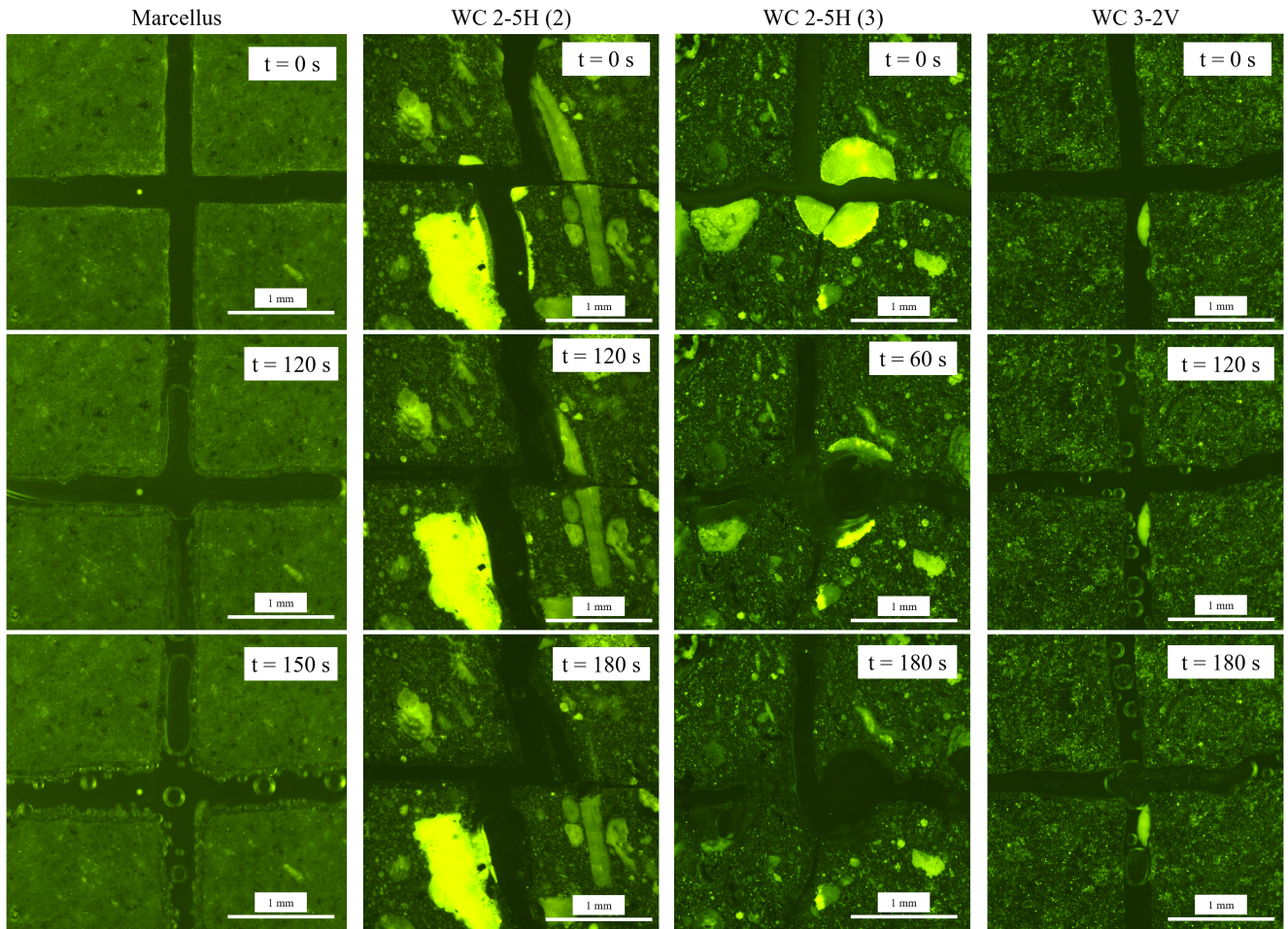


Fig. 2. Dynamic dissolution images for three different samples at different time instance (image width = 3 mm).

201 that are controlled by the coupling between reaction, heterogeneity and advective
 202 transport. To analyze quantitatively these images, we track the evolution of integral
 203 geometric quantities (fracture volume and interface length) as reaction progresses.
 204 Specifically, we define the normalized fracture volume (Ψ) as

$$\Psi(t) = \frac{V(t)}{V_0},$$

205 where $V(t)$ is the fracture volume at each time interval, and V_0 is the total volume
 206 of the sample, $V_0 = 3 \times 3 \times 0.2 = 1.8 \text{ mm}^3$. Because the fractured sample is quasi-
 207 two-dimensional, with the image being the focusing plane, we define a normalized
 208 solid-fracture interface length $\Gamma(t)$, rather than an interface area, as

$$\Gamma(t) = \frac{L(t)}{L_0},$$

where $L(t)$ is the interface length at each time instance, and L_0 is the interface

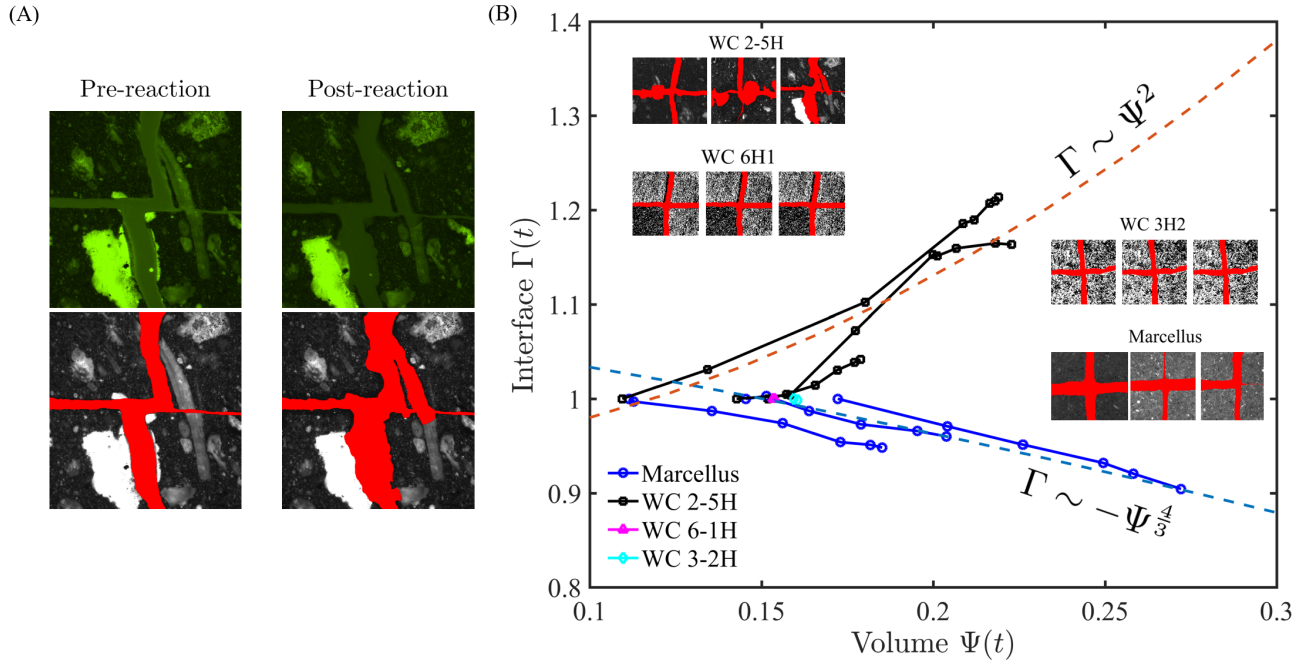


Fig. 3. Image characterization of fracture porosity and its evolution. (A) Example fluorescent images of dye-filled fractures pre- and post-reaction (WC 2-5H(3)). In the second row, fracture space is segmented from the surrounding rock (as shown in red) in processed fluorescent images. The segmented region is used to calculate normalized fluid volume (Ψ) and the interface fracture length, Γ , with time. (B) Evolution of fracture volume and solid-fracture interface lengths with reaction time. Results of three replicate experiments for WC 2-H and Marcellus are plotted using the corresponding Ψ and Γ at each time interval. The dashed blue line shows the scaling of Equation (1), specifically $\Gamma = 1.08 - \Psi^{4/3}$. The dashed red line is $\Gamma = 0.65 + \Psi^{1/2}$. Processed images are included. Original images are in the SI, Figures S8 and S9.

209

210 length at time $t = 0$ s. This quantity provides information about the evolution
 211 of interfacial length during reactions. When $\Gamma(t) > 1$ for $t > t_0$, new interface is
 212 generated as a result of the dissolution process. If $\Gamma(t) < 1$ for $t > t_0$ the interface
 213 length is decreasing, i.e. the interface is becoming smoother. If $\Gamma(t) \approx 1$ for
 214 $t > t_0$, then the fracture interface length remains approximately constant during
 215 dissolution. The area (used to calculate the volume as pore area multiplied by
 216 the depth (0.2 mm)) and interface lengths are measured using image segmentation
 217 and the edge detection tool in ImageJ (Figure 3(A)). In Figure 3(B), we plot the
 218 calculated $\Gamma(t) - \Psi(t)$ correlations as time progresses for all samples and their replicas
 219 (symbols connected by solid lines). Figure 3(B) shows that $\Gamma(t)$ and $\Psi(t)$ can be
 220 either positively correlated, negatively correlated, or remain constant as time evolves,
 221 i.e. $((\Gamma(t), \Psi(t)) = (\Gamma(t_0), \Psi(t_0)))$, depending on the carbonate content of the sample
 222 (or alternatively, the characteristic length scale of the carbonate heterogeneity).
 223 Specifically, all Marcellus samples ($\ell \gg L$) exhibit a negative correlation between Γ
 224 and Ψ , i.e. $d\Gamma/d\Psi < 0$, with Γ decreasing as fracture volume Ψ increases during
 225 dissolution ($t > t_0$). Instead the Wolfcamp samples with intermediate carbonate
 226 content ($\ell \sim L$) have a positive correlation between Γ and Ψ , i.e. $d\Gamma/d\Psi > 0$,
 227 with Γ increasing as fracture volume Ψ increases during dissolution ($t > t_0$). The

228 changes in normalized surface length for the high to medium carbonate content
229 can be significant and in the $\pm 20\%$ range. Fracture volume can also significantly
230 change with variations up to 25-100 %. The slopes of $\Gamma - \Psi$ curves for the Marcellus
231 and the WC2-5H samples in Figure 3(B) are similar for each sample set, indicating
232 that the reaction rate of calcite is approximately the same among samples with
233 similar carbonate content: **the dissolution reaction rate is not limited by reactive
234 minerals in the Marcellus samples, i.e., the time-scale of the reaction is dominated
235 by the reaction rate of pure calcite.** Because at high Péclet numbers, mass transport
236 **is controlled by advection**, the greatest discrepancies in each class are caused by
237 heterogeneities in the spatial distribution of reactive minerals (see e.g. WC 2-5H
238 curves) **and their accessibility to the connected pore-space.** Starkly different is the
239 behavior of the carbonate poor samples (WC 6H1 and WC 3H2) for which no change
240 in either fracture surface area nor fracture volume can be detected at this scale
241 (mm). In the following section, pre- and post-reaction SEM and EDS measurements
242 are employed to probe the impact of transport at scales that are relevant to reactive
243 processes (μm) to elucidate the interplay between spatial chemical heterogeneity
244 and topological changes of the reacting interface.

245 **Static Results.** Figure 4 shows the pre-reaction SEM-BSE photomicrographs with
246 the areas of interest highlighted in blue boxes (row A), pre-reaction composite
247 elemental maps compiled using EDS data for the select region (row B), post-
248 reaction SEM-BSE images of the same regions (row C), and corresponding post-
249 reaction composite elemental maps (row D). Full-scale SEM-BSE and EDS images
250 (composites and individual elements) showing all four quadrants are included in the
251 Supporting Information.

252 **Carbonate-poor samples.** For the carbonate-poor samples (WC 3-2V and WC 6-1H,
253 8 and 21 wt % respectively), small calcite (red) and dolomite (purple) particles are
254 distributed throughout as apparent in the pre-reaction EDS images (Figure 4(B)).
255 Although no large-scale topological alterations are detected from the dynamic-image
256 analysis (as discussed in the previous section), surface carbonates dissolve when
257 reactive fluids come in contact with the fracture surface. Dissolution continues until
258 a reacted zone forms on and adjacent to the fracture walls creating micron-sized
259 ($\sim 1\text{-}10\ \mu\text{m}$) moldic pores that correspond to dissolved calcite and dolomite grains
260 (Figures 4(B-C)). This results in topological alterations of the physical interface
261 that are undetected at a larger scale (e.g. surface roughness and fracture volume),
262 while its chemical composition is altered at the mm scale through the formation of
263 a reacted interface zone. **Figure 4 shows that, in the WC 6-1H sample, the pores
264 created adjacent to the surface are due to dissolution of calcite and dolomite, while
265 further from the surface only calcite grains are dissolved.** This result indicates that

266 different reactivity between minerals may create a layered structure, which should
267 be taken into account in reactive transport studies. Comparing the WC 3-2V and
268 the WC 6-1H samples with the sample with greater carbonate content (WC 2-5H),
269 the WC 2-5H shows larger moldic pores and pathways where elongated grains are
270 dissolved, while the former samples contain moldic pores only. In addition to the
271 generation of moldic micro-pores shown in Figure 4, substantial changes in the
272 width, shape, and tortuosity of the fractures are caused by dissolution as the size of
273 calcite and dolomite particles increases.

274 **Samples with intermediate carbonate content.** The heterogeneous WC 2-5H sample
275 (65 wt % in carbonate content) contains mainly calcite (red in Figure 4-B) with
276 dolomite (purple) locally distributed in silicate-rich (green) regions. Relatively
277 non-reactive minerals formerly embedded within the calcite matrix are exposed by
278 dissolution, including quartz, albite, and other silicates (green in Figure 4-D). The
279 morphology of these grains can range from euhedral to subhedral quartz and albite
280 (inserts in Figure 4-C). In the WC 2-5H samples, compositional heterogeneities
281 are reflected in the dissolution patterns. During reactive flow, the heterogeneous
282 distribution of calcite in WC 2-5H leads to a significant (macroscopic) alteration
283 of the fracture profile as indicated by the dashed region in Figure 4-C for the
284 sample. This is consistent with an increase in the interface area as dissolution
285 proceeds, as highlighted by the positive correlations between Ψ and Γ , measured
286 from dynamics image analysis (Figure 3-B). This affects subsequent reactive flow
287 and transport processes as documented in the dynamic image data. Additionally, by
288 comparing the pre- and post-reaction sample saturated with dye and their processed
289 equivalents (Figure 3-A), a sliver of non-reactive matrix that was attached to the
290 elongated calcite fossil remains unsupported and potentially movable after the fossil
291 dissolved completely. This suggests that large unreacted grains may be mobilized as
292 a result of differential dissolution. Moreover, the WC 2-5H samples have a greater
293 solid-fluid interface during the dissolution both at the fracture (Figure 3) and pore
294 (Figure 4) scales. Additionally, in the WC 2-5H samples, the non-reactive portion
295 consisting of silicates and OM is heterogeneously distributed. The greater continuity
296 of the non-reactive silicates requires more extensive calcite dissolution to allow
297 particles being exposed to the fluid and potentially mobilized.

298 **Carbonate-rich samples.** In the carbonate-rich samples (Marcellus, 86 wt %), calcite
299 (red) and minor amounts of silicate minerals (green) are homogeneously distributed
300 (Figure 4-B). Unlike the other three samples, the carbonate-rich Marcellus sample
301 does not exhibit a defined altered zone (Figure 4-Marcellus row (C)). When disso-
302 lution occurs, the reaction is concentrated along the entire fracture surface, and
303 moldic pores and elongated pathways do not form as in other samples. Instead, SEM

304 results show that dissolution at the fracture surface in the carbonate-rich Marcellus
 305 sample uniformly reduces the length of the solid-fracture interface, therefore leading
 306 to negative $\Gamma - \Psi$ correlations as dissolution proceeds (Figure 3-B). Pre-reaction
 307 EDS and BSE-SEM images (Figure 4-B)) show that non-reactive particles (silicates)
 308 embedded in the calcite matrix are distributed homogeneously in the entire sample.
 309 In the post-reaction composite EDS image, silicate minerals (green) are uniformly
 310 exposed on the fracture wall by dissolution of the surrounding calcite (red in Figure
 311 4-D). These non-reactive particles remained attached to and/or are embedded in
 312 the fracture surface.

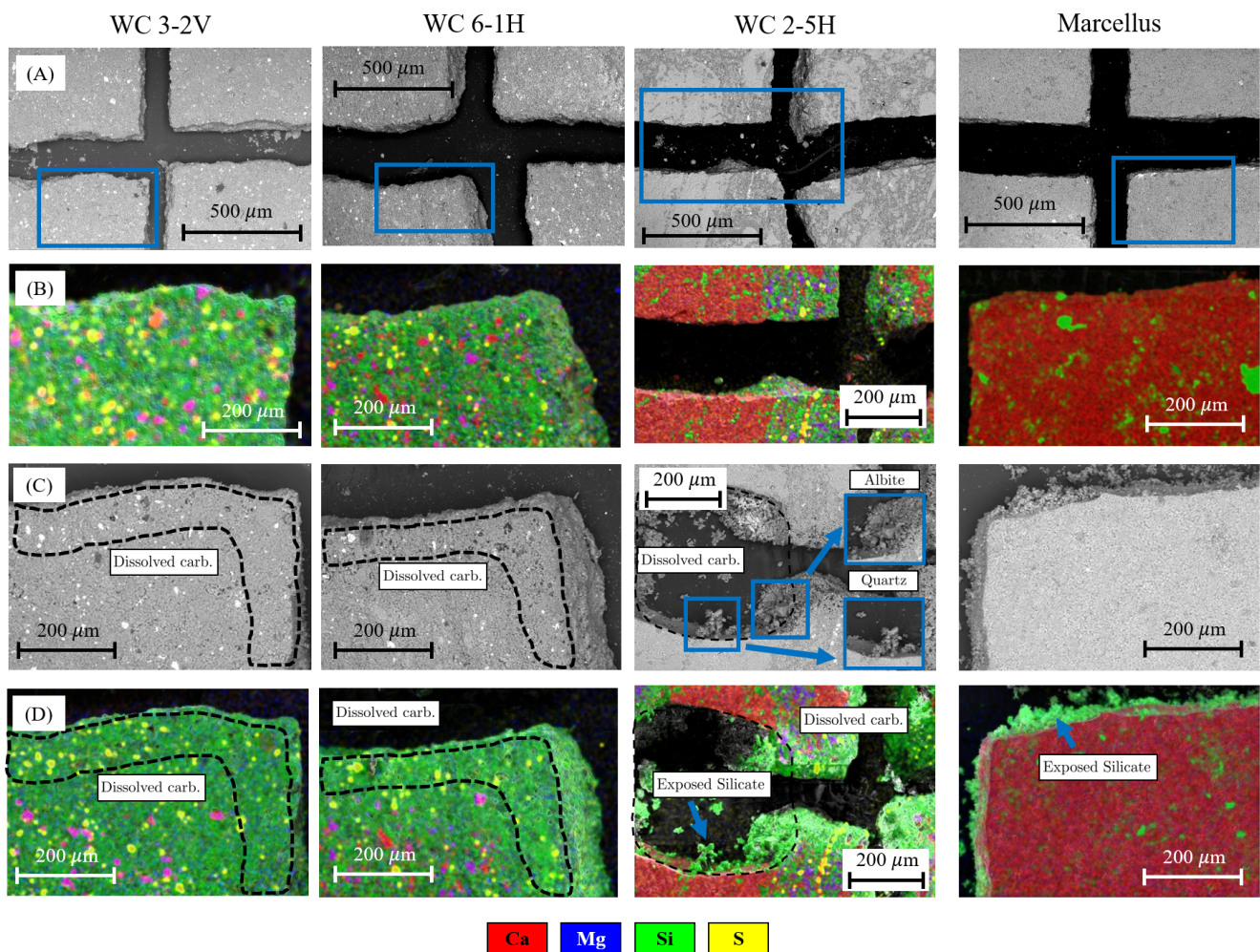


Fig. 4. (A) Pre-reaction SEM-BSE images of the four samples (image width = 1.38 mm). Blue boxes (image width ~ 0.5 mm) correspond to select regions of pre-reaction EDS, post-reaction SEM-BSE, and post-reaction EDS images in rows B, C, and D. (B) Pre-reaction composite elemental maps for the select region. (C) Post-reaction SEM-BSE images of the same region. (D) Corresponding post-reaction composite elemental maps. Samples are ordered from carbonate-poor on the left to carbonate-rich on the right. The carbonate dissolution zones with newly developed porosity are indicated by dashed lines. The dashed region for WC 2-5H corresponds to calcite dissolved from both sides of the fracture. In this sample, calcite dissolution exposed euhedral quartz and albite. Fine-grained silicates are also exposed by calcite dissolution in the Marcellus sample. The colors indicate individual elements as listed in the legend for each composite element image. Full-size composite elemental images and SEM-BSE images are in the Supporting Information (S4-S7).

313 **Implications for Reactive Transport Modeling and Reactivity Assessment.** The
314 unique ability to combine SEM-BSE and EDS images of the same sample pre- and
315 post-reaction, as well as in-operando time-resolved optical measurements during
316 dissolution, provides the opportunity to quantify the impact of carbonates spatial
317 heterogeneity and their accessibility to connected pore-space on reaction rates at a
318 given flow rate. Quantitative estimates of the temporal evolution of mineral surface
319 area in terms of porosity are at the foundation of a number of broadly used reactive
320 transport codes, such as CrunchFlow, where reactivity is expressed in terms of a
321 single value of mineral reactive surface area, A :

$$R = Akf_e,$$

322 where k is the reaction rate constant, and f_e is a function of Gibbs free energy or the
323 thermodynamic driving force (16). Discrepancies between mineral dissolution rates
324 observed in laboratory experiments versus natural samples have been attributed,
325 among others, to porous medium effects, where the accessibility of reactive mineral
326 surfaces (e.g. carbonates) may be strongly controlled by their spatial distribution
327 relative to the connected pore structure (16). For real rock samples, the assumption
328 that A is the same as that of the pure reactive substance may require adjustments
329 by scaling factors of various orders of magnitude ($10^{-3} - 10^{-1}$). A number of studies
330 have emphasized the difficulty in estimating and constraining reactive surface
331 area for reactive transport codes (16, 17). **Geometry-based methods are widely**
332 **applied where minerals are assumed to have simple geometries.** As a result, during
333 dissolution processes, the temporal evolution of mineral surface area is generally
334 captured through (17, Eq.(2))

$$A(t) = A^i \left(\frac{\phi_m(t)}{\phi_m^i} \right)^{\frac{2}{3}} \left(\frac{\phi(t)}{\phi^i} \right)^{\frac{2}{3}},$$

335 where ϕ_m is the reactive mineral volume fraction, and ϕ is the porosity. The
336 superscript “ i ” refers to the corresponding quantity evaluated at $t = 0$. For the
337 set of experiments with Marcellus samples (high carbonate content), $\phi_m(t)$ can be
338 approximated as $\phi_m(t) \approx \phi^e - \phi(t)$ where ϕ^e is the porosity evaluated at the end of
339 the experiment $\phi^e = \phi(t_{end})$. Then, the previous model can be recast in terms of Γ
340 and Ψ as follows

$$\Gamma(t) = \left(\frac{\Psi(t_{end}) - \Psi(t)}{\Psi(t_{end}) - 1} \right)^{\frac{2}{3}} \Psi(t)^{\frac{2}{3}},$$

341 since $\Gamma(t) = A(t)/A^i$ and $\Psi(t) = \phi(t)/\phi^i$, when the sample is quasi two-dimensional.
342 This leads to the following scaling relationship

$$\Gamma \sim -\Psi^{\frac{4}{3}}. \quad [1]$$

343 Figure 3(B) shows that Eq. (1) (dashed blue line) correctly captures the experimental
344 trend for the Marcellus samples, in which (i) an increase in porosity leads to a
345 decrease in surface area (due to grains becoming more round as dissolution progresses)
346 and (ii) there is no limitation in reactive area accessibility to the connected pore-
347 space, where the acid flows (i.e. porous media effects are negligible). This result
348 also shows that, in this setup, 3D effects can be neglected to leading order, when
349 estimating $A - \phi$ trends. Instead, for WC 2-5H samples (as well as for low carbonate
350 samples), the correlation between Γ and Ψ significantly deviates from Eq. (1):
351 from the experiments on WC 2-5H samples, a scaling relationship of $\Gamma \sim \Psi^{1/2}$
352 (dashed red line) can be extracted (where Γ now refers to the total surface area).
353 Such a scaling is able to capture an increase in surface area during dissolution
354 due to surface roughening caused by the spatial distribution of carbonate grains
355 inclusions as well as their limited accessibility to the connected pore structure,
356 where acid is flowing. However, more complex correlations may be warranted
357 to account for additional effects (e.g. achievement of a plateau at finite times).
358 Scaling laws that deviate from those theoretically predicted by Eq. (1) can be traced
359 back to the highly nonlinear temporal evolution of both surface area and porosity
360 during dissolution, as shown in Figure S16 in SI, compared to a linear behavior
361 observed in the Marcellus samples. Such nonlinearities can be primarily attributed
362 to accessibility limitations of reactive surfaces to the connected pore space, i.e. to
363 the spatial distribution and characteristic size of carbonate inclusions, which, in
364 turn, are function of carbonate content. These observations suggest that, for these
365 samples, carbonate content can be used as an a priori proxy to assess potential
366 impact of porous medium effects on reactive transport rates at a fixed flow rate.
367 This analysis shows how the experimental framework developed in this work can (i)
368 be directly used to constrain $A - \phi$ correlations in reactive transport models (at
369 fixed flow rate), and (ii) inform the development of new dynamic correlations for
370 natural samples with different composition, in which porous medium effects become
371 predominant due to the spatial heterogeneity of the reactive minerals and their
372 accessibility to the connected pore structure. Note that the combination of optical
373 measurements with compositional analysis enables us, on the one hand, to extract
374 $A - \phi$ correlations based on total surface area (rather than reactive area) therefore
375 potentially simplifying image analysis and, on the other hand, to perform a more
376 detailed analysis tracking specific minerals.

377 Conclusions

378 We investigated dissolution of real geological samples using a newly developed
379 microfluidic experimental platform that allows for static characterization at the
380 micro- and sub-micrometer scale and dynamic characterization at the millimeter
381 scale.

382 We tested eight (including four repeated experiments) shale reservoir rock samples
383 with a range of reactive mineral concentrations and microstructures. We injected
384 1 % HCl as an acidic fluid. We conducted SEM imaging to characterize the
385 static pre- and post-reaction samples, and collected EDS data to detect changes
386 in composition before and after dissolution. All of the pre-, concurrent, and post-
387 reaction measurements were correlated to achieve detailed characterization of the
388 same regions of interest at different scales ranging from the mm to the μm . This
389 protocol allows us to trace accurately dissolution of calcite and dolomite, exposure
390 of non-reactive particles, structural changes at the fracture and pore scales, solid-
391 fracture interface and fracture volume trends, and mineral compositions at the same
392 locations.

393 For samples with less than 30% carbonate (WC 3-2V and WC 6-1H), reactive
394 minerals (calcite and dolomite) are present as small grains and distributed homoge-
395 neously in the entire sample. Although their dissolution leaves small moldic pores
396 in the matrix ($\sim 1 - 100 \mu\text{m}$), the matrix does not lose its integrity because of
397 the presence of surrounding silicates; as a result, the fracture geometry remains
398 substantially unaffected at the mm scale, leading to constant values of fracture
399 volume and interface area during the dissolution process. For the samples with
400 intermediate carbonate content (20-65 %), reactive calcite occurs as large grains
401 that are distributed heterogeneously. When exposed to reactive fluids, large voids
402 develop as the calcite is selectively dissolved. This leads to an increase in frac-
403 ture surface and volume as dissolution proceeds, i.e. in positive fracture-surface
404 versus fracture-volume correlations in Figure 3(B), which can be quantified by
405 dynamic-image analysis at the mm scale. For the carbonate-rich Marcellus samples,
406 fracture volume increases due to the uniform widening of pre-existing fractures,
407 which also reduces the overall interface length, leading to negative fracture-surface
408 versus fracture-volume correlations as dissolution proceeds. These newly obtained
409 observations are critical to assess the temporal scales of natural dissolution and
410 optimize geological engineering applications. [The high temporal resolution data,](#)
411 [combined with compositional analysis, provides a new workflow for estimating](#)
412 [reactivity of real rock samples by quantifying the temporal correlation between](#)
413 [surface area and pore volume during dissolution. Specifically, deviations from theo-](#)
414 [retically postulated correlations can be quantified and traced back to the temporally](#)
415 [nonlinear evolution of surface area and porosity during dissolution for samples in](#)

416 which intermediate carbonate content and its heterogeneous distribution translates
417 into limitations in reactive surface accessibility to the connected pore space (i.e.
418 significant porous media effects due).

419 Additionally, the use of both dynamic and static measurements shows that non-
420 reactive particles are exposed at different rates, depending on their composition,
421 distribution, the fracture volume, and the solid-fluid interface length behavior as
422 dissolution progresses. To the best of our knowledge, these data are the first to
423 show different possible mechanisms associated with exposure of unreacted fines: 1)
424 constant exposure of small nonreactive particles embedded in the calcite matrix
425 (Figure 4-D Marcellus) and 2) complete dissolution of large calcite grains which
426 might lead to weakening and mobilization of portions of the matrix itself (Figure 4-D
427 WC 2-5H). In particular, the dynamic results suggest that small particles are exposed
428 constantly during dissolution of the carbonate-rich sample. The matrix weakening
429 requires longer exposure times, results in significant changes of the fracture structure,
430 and it may cause fracture collapse for heterogeneous samples with intermediate
431 carbonate content. It is worth pointing out that the presence of non-reactive
432 particles was detected both in the effluent as well as on the PDMS surface, in
433 the proximity of the fracture surface, after dissolution. This suggests that, at this
434 Péclet number, dissolution-driven mechanical erosion (i.e. loosening of particles
435 and entrainment by the flow) may lead to nonreactive particle displacement and
436 consequent pore-clogging.

437 Our study demonstrates the potential and multifunctional nature of this novel
438 platform of sample-embedded microfluidic for studying the dynamics of geochemi-
439 cal reactions and its direct application to constrain reactive transport models by
440 extracting a relationship $\Gamma \sim f(\Psi)$ using high temporal resolution data achieved
441 by microfluidics. Also, the ability to track in time, at high temporal resolution,
442 the evolution of (and correlation between) fracture volume and solid-fracture in-
443 terface length might prove very insightful in the identification and quantification
444 of (precursors of) instabilities, i.e. wormholes, as well as other complex feedbacks
445 between mineral dissolution, flow and transport, under different dynamic conditions
446 (i.e. Pe). The combination of static and dynamic measurements on the sample
447 allows one to explore the mechanisms and the synergy of reactive transport, flow,
448 and geochemistry at multiple scales.

449 **ACKNOWLEDGMENTS.** This work was supported as part of the Center for Mechanistic
450 Control of Unconventional Formations (CMC-UF), an Energy Frontier Research Center funded
451 by the U.S. Department of Energy (DOE), Office of Science, Basic Energy Sciences (BES), under
452 Award # DE-SC0019165. Part of this work was performed at the Stanford Nano Shared Facilities,
453 supported by the National Science Foundation under award ECCS-2026822.

454 1. ML Frezzotti, J Selverstone, ZD Sharp, R Compagnoni, Carbonate dissolution during subduction revealed by diamond-bearing rocks from the Alps. *Nat. Geosci.* 4, 703–706 (2011).

- 455 2. O Sulpis, BP Boudreau, A Mucci, C Jenkins, RM Key, Current CaCO₃ dissolution at the seafloor caused by anthropogenic CO₂. *Proc. Natl. Acad. Sci.* **115** (2018).
- 456 3. JP Fitts, CA Peters, Caprock fracture dissolution and CO₂ leakage. *Rev. Mineral. Geochem.* **77**, 459–479 (2013).
- 457 4. AL Harrison, et al., Element release and reaction-induced porosity alteration during shale-hydraulic fracturing fluid interactions. *Appl. Geochem.* **82**, 47–62 (2017).
- 458 5. C Noiriél, B Madé, P Gouze, Impact of coating development on the hydraulic and transport properties in argillaceous limestone fracture. *Water Resour. Res.* **43** (2007).
- 459 6. C Wang, et al., An invisible soil acidification: Critical role of soil carbonate and its impact on heavy metal bioavailability. *Sci. reports* **5**, 1–9 (2015).
- 460 7. M Konrad-Scholke, et al., Mineral dissolution and reprecipitation mediated by an amorphous phase. *Nat. Commun.* **9** (2018).
- 461 8. BR Ellis, et al., Dissolution-driven permeability reduction of a fractured carbonate caprock. *Environ. Eng. Sci.* **30**, 187–193 (2013).
- 462 9. Surface Reactive Fluid's Effect on Shale, SPE Oklahoma City Oil and Gas Symposium / Production and Operations Symposium Vol. All Days, (2007) SPE-106815-MS.
- 463 10. H Aljamaan, CM Ross, AR Kovscek, Multiscale imaging of gas storage in shales. *SPE J.* **22**, 1–760 (2017).
- 464 11. Y Gensterblum, et al., Gas transport and storage capacity in shale gas reservoirs—A review. Part A: Transport processes. *J. Unconv. Oil Gas Resour.* **12**, 87–122 (2015).
- 465 12. KS Lee, TH Kim, *Transport in Shale Reservoirs*. (Gulf Professional Publishing, Cambridge), (2019).
- 466 13. SS Morsy, JJ Sheng, MY Soliman, *Improving Hydraulic Fracturing of Shale Formations by Acidizing*. (Improving Hydraulic Fracturing of Shale Formations by Acidizing), (2013).
- 467 14. JA Hakala, et al., Laboratory-scale studies on chemical reactions between fracturing fluid and shale core from the Marcellus Shale Energy and Environmental Laboratory (MSEEL) Site. (Unconventional Resources Technology Conference), (2017).
- 468 15. Q Li, AD Jew, GE Brown Jr, JR Bargar, K Maher, Reactive transport modeling of shale–fluid interactions after imbibition of fracturing fluids. *Energy & Fuels* **34**, 5511–5523 (2020).
- 470 16. LE Beekingham, et al., Evaluation of mineral reactive surface area estimates for prediction of reactivity of a multi-mineral sediment. *Geochimica et Cosmochimica Acta* **188**, 310–329 (2016).
- 471 17. F Qin, LE Beekingham, The impact of mineral reactive surface area variation on simulated mineral reactions and reaction rates. *Appl. Geochem.* **124**, 104852 (2021).
- 472 18. V Vishai, et al., Interpreting pore dimensions in gas shales using a combination of SEM imaging, small-angle neutron scattering, and low-pressure gas adsorption. *Energy & Fuels* **33**, 4835–4848 (2019) Publisher: American Chemical Society.
- 474 19. Y Zhang, TJ Barber, Q Hu, M Bleuel, HF El-Sobky, Complementary neutron scattering, mercury intrusion and SEM imaging approaches to micro- and nano-pore structure characterization of tight rocks: A case study of the Bakken shale. *Int. J. Coal Geol.* **212**, 103252 (2019).
- 475 20. L Frouté, AR Kovscek, Nano-imaging of shale using electron microscopy techniques in *Proceedings of the Unconventional Resources Technology Conference (URTeC)*. (Society of Petroleum Engineers, Virtual), (2020).
- 476 21. CJ Werth, C Zhang, ML Brusseau, M Oostrom, T Baumann, A review of non-invasive imaging methods and applications in contaminant hydrogeology research. *J. Contaminant Hydrol.* **113**, 1–24 (2010).
- 480 22. DC Joy, Scanning electron microscopy for materials characterization - sciencedirect. *Curr. Opin. Solid State & Mater. Sci.* **2**, 465–468 (1997).
- 481 23. C Soulaïne, S Roman, A Kovscek, HA Tchelepi, Mineral dissolution and wormholing from a pore-scale perspective. *J. Fluid Mech.* **827**, 457–483 (2017).
- 482 24. H Yoon, KN Chojnicki, MJ Martinez, Pore-scale analysis of calcium carbonate precipitation and dissolution kinetics in a microfluidic device. *Environ. Sci. & Technol.* **53**, 14233–14242 (2019).
- 483 25. J Poonosamy, et al., A microfluidic experiment and pore scale modelling diagnostics for assessing mineral precipitation and dissolution in confined spaces. *Chem. Geol.* **528**, 119264 (2019).
- 484 26. W Song, F Ogunbanwo, M Steinsbø, MA Fernø, AR Kovscek, Mechanisms of multiphase reactive flow using biogenically calcite-functionalized micromodels. *Lab on a Chip* **18**, 3881–3891 (2018).
- 485 27. D Ross, RM Bustin, The importance of shale composition and pore structure upon gas storage potential of shale gas reservoirs. *Mar. & Petroleum Geol.* **26**, 916–927 (2009).
- 486 28. T Saif, Q Lin, AR Butcher, B Bijeljic, MJ Blunt, Multi-scale multi-dimensional microstructure imaging of oil shale pyrolysis using X-ray micro-tomography, automated ultra-high resolution SEM, MAPS mineralogy and FIB-SEM. *Appl. Energy* **202**, 628–647 (2017).
- 488 29. DM Wang, YM Xu, DM He, J Guan, OM Zhang, Investigation of mineral composition of oil shale. *Asia-Pacific J. Chem. Eng.* **4**, 691–697 (2009).
- 489 30. G Kosakowski, B Berkowitz, Flow pattern variability in natural fracture intersections. *Geophys. Res. Lett.* **26**, 1765–1768 (1999).
- 490 31. A Dahi Taleghani, JE Olson, How natural fractures could affect hydraulic-fracture geometry. *SPE J.* **19**, 161–171 (2013) Publisher: Society of Petroleum Engineers.
- 491 32. O Kolawole, I Ispas, Interaction between hydraulic fractures and natural fractures: Current status and prospective directions. *J. Petroleum Explor. Prod. Technol.* **10**, 1613–1634 (2020).
- 492 33. JFW Gale, SE Laubach, JE Olson, P Eichhubl, A Fall, Natural fractures in shale: A review and new observations. *AAPG Bull.* **98**, 2165–2216 (2014).
- 493 34. H Wen, L Li, D Crandall, A Hakala, Where lower calcite abundance creates more alteration: Enhanced rock matrix diffusivity induced by preferential carbonate dissolution. *Energy & Fuels* **30**, 4197–4208 (2016).
- 495 35. H Fazeli, M Nooraiepour, H Hellevang, Microfluidic study of fracture dissolution in carbonate-rich caprocks subjected to CO₂-charged brine. *Ind. & Eng. Chem. Res.* **59**, 450–457 (2019).
- 496 36. H Deng, JP Fitts, RV Tappero, JJ Kim, CA Peters, Acid erosion of carbonate fractures and accessibility of arsenic-bearing minerals: In operando synchrotron-based microfluidic experiment. *Environ. Sci. & Technol.* **54**, 12502–12510 (2020).
- 498 37. CT Gerold, AT Krummel, CS Henry, Microfluidic devices containing thin rock sections for oil recovery studies. *Microfluid. Nanofluidics* **22**, 1–7 (2018).
- 499 38. M Nooraiepour, H Fazeli, R Miri, H Hellevang, Effect of CO₂ phase states and flow rate on salt precipitation in shale caprocks—a microfluidic study. *Environ. Sci. & Technol.* **52**, 6050–6060 (2018).
- 500 39. C Zhang, M Oostrom, TW Wietsma, JW Grate, MG Warner, Influence of viscous and capillary forces on immiscible fluid displacement: Pore-scale experimental study in a water-wet micromodel demonstrating viscous and capillary fingering. *Acta Ophthalmol.* **25**, 3493–3505 (2011).
- 501 40. B Ling, HJ Khan, JL Druhan, I Battiato, Multi-scale microfluidics for transport in shale fabric. *Energies* **14**, 1–23 (2020).
- 502 41. B Ling, J Bao, M Oostrom, I Battiato, AM Tartakovsky, Modeling variability in porescale multiphase flow experiments. *Adv. Water Resour.* **105**, 29–38 (2017).
- 503 42. S Molins, et al., Simulation of mineral dissolution at the pore scale with evolving fluid-solid interfaces: Review of approaches and benchmark problem set. *Comput. Geosci.* **25**, 1285–1318 (2021).